



Atomic resolution transmission electron microscopy visualisation of channel occupancy in beryl in different crystallographic directions

Carina Silke Hanser¹ · Per Erik Vullum² · Antonius Theodorus Johannes van Helvoort³ · Fabian Dietmar Schmitz^{1,4} · Tobias Häger¹ · Roman Botcharnikov¹ · Bodil Holst⁵

Received: 15 December 2023 / Accepted: 12 June 2024 / Published online: 5 July 2024
© The Author(s) 2024

Abstract

The causes of colour in beryl have been a research topic for decades. For some varieties, such as emerald (green, coloured by Cr^{3+} and/or V^{3+}), the main cause of colour is substitutions by metal atoms within the framework. However, the causes for the yellow and blue colours in heliodor, golden beryl and aquamarine are still debated. It is generally agreed that Fe ions are responsible for the colour, but there are differing conclusions about the valence states of these ions, the occupied positions and the colour-inducing processes involved. The colour of aquamarine is commonly attributed to intervalence charge transfer (IVCT) between Fe^{3+} and Fe^{2+} . Various combinations of sites have been proposed to host the Fe ions engaging in this IVCT. Here we present a new approach to address the topic of colour generation: atomic resolution scanning transmission electron microscopy (STEM). For the first time, atomic resolution images of a beryl (natural aquamarine) are presented in the three crystallographic directions [0001], [1-210] and [1-100]. Ions are clearly resolved in the channels. From the ratio of channel occupation and the correlation of the atoms per formula unit (apfu) calculations we conclude that Fe resides in the framework, not in the channels. The projections in the [1-210] direction directly show that the cavity channel site $2a$ is occupied, most likely by Cs, in agreement with recent results in the literature.

Keywords Beryl · HAADF STEM · Iron ions · Channel occupation/occupancy · Caesium ions

Introduction

The crystal structure of beryl ($\text{Be}_3\text{Al}_2[\text{Si}_6\text{O}_{18}]$) was first identified in a publication by Bragg and West in 1926 (Bragg and West 1926; Hawthorne and Černý 1977). Its space group was determined to be $P6/mcc$ and the hexagonal structure was later refined and amended in the course of the following decades (see e.g. Gibbs et al. 1968; Morosin 1972; Artioli et al. 1993). The framework of beryl was first visualised by transmission electron microscopy (TEM) in a study by Buseck and Sumio (1974). Al is present in an octahedral coordination with O atoms within beryl, Be and Si are tetrahedrally coordinated (Fig. 1a). The Si tetrahedra combine to form six-membered rings, which characterise beryl as a cyclosilicate. Successive layers of these rings perpendicular to the c -axis create open channels in the crystal structure (Fig. 1b). These channels can be occupied by a variety of ions and molecules, such as alkalis, H_2O or CO_2 . The incorporation of transition metal ions, such as Cr and/or V in emerald (a green beryl variety) or Mn in red beryl or morganite (red and pink beryl varieties), by ionic

Fabian Dietmar Schmitz and Bodil Holst contributed equally to this work.

✉ Carina Silke Hanser
chanser@uni-mainz.de

- ¹ Institute of Geosciences, Johannes Gutenberg-University Mainz, J.-J.-Becher-Weg 21, 55128 Mainz, Germany
- ² SINTEF Industry, Høgskoleringen 5, 7034 Trondheim, Norway
- ³ Department of Physics, Norwegian University of Science and Technology (NTNU), Høgskoleringen 5, 7034 Trondheim, Norway
- ⁴ RheinMainGemConsulting, Forsterstraße 4, 55118 Mainz, Germany
- ⁵ Department of Physics and Technology, University of Bergen, Allegaten 55, 5007 Bergen, Norway

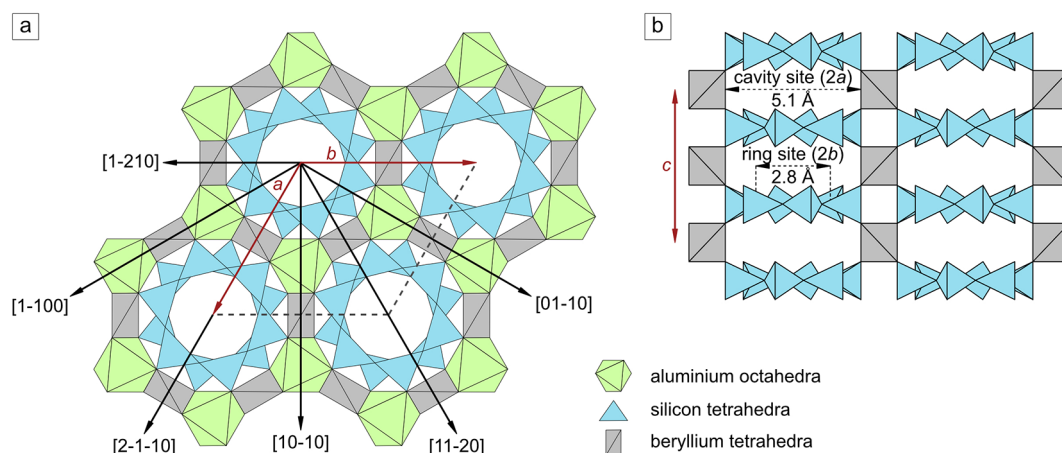


Fig. 1 **a** The structure of beryl viewed down the c -axis (along the [0001] direction). Basic crystallographic directions are shown with black arrows and associated indices. The a - and b -axes are marked with red arrows. The rhombus shape (spanning between the axes a and b and the dashed line) indicates the unit cell. **b** The structure of beryl as seen perpendicular to the c -axis of the crystal (along the a - or b -axes). The c -axis is indicated by the red arrow. For better overview purposes only the Si and some of the Be tetrahedra are shown. Two sites are

substitution of Al in the framework is widely accepted to be the cause for the colour of these beryl varieties (e.g. Nassau and Wood 1968; Nassau 1978; Andersson 2013; Fridrichová et al. 2018). It is also known that yellow (heliodor and golden beryl) and blue colours (aquamarine) are caused by Fe ions. Yellow and blue colours in beryl have previously been linked to high, relative amounts of Fe^{3+} and Fe^{2+} , respectively (Viana et al. 2002) and the electronic interactions (mainly charge transfers) these ions can undergo (Nassau 1978; Fritsch et al. 1988; Burns 1993; Mathew et al. 2000). Furthermore, mixed greenish colours, which are caused by Fe rather than Cr and/or V (as in emerald), also exist (Mathew et al. 2000). In contrast to other transition metal ions, however, there is still considerable debate about which possible positions Fe ions can occupy within beryl. Fe ions have been proposed to be able to substitute for Al, Be, and Si (Viana et al. 2002; Fridrichová et al. 2015; Andersson 2019). Furthermore, several studies suggest Fe ions could be present inside the channels (e.g. Wood and Nassau 1968; Goldman et al. 1978; Blak et al. 1982; Přikryl et al. 2014; Arivazhagan et al. 2017; Bačik and Fridrichová 2019; Bunnag et al. 2020; Shang et al. 2022). However, others do not, or not entirely, uphold this interpretation as, for instance, no Fe was identified in the channels (Spinolo et al. 2007; Andersson 2013) or only part of their data allow the interpretation of Fe possibly residing in the channel, while the rest of their results are not in agreement with it (Groat et al. 2010).

In a previous study by Arivazhagan et al. (2017), a heliodor (yellow beryl) was analysed using aberration corrected atomic resolution scanning transmission electron

distinguished in the channels. The site $2a$ is located at the level of the Be tetrahedra and the Al octahedra and is the larger of the two sites with an approximate diameter of 5.1 Å, thus also called the cavity site. The smaller site $2b$, with an approximate diameter of 2.8 Å, is located between the Si tetrahedra rings and is therefore also referred to as the ring site (modified after Łodziński et al. 2005; Gaudry et al. 2007; Taran and Vyshnevskiy 2019; Wang et al. 2021)

microscopy (STEM). Images were obtained in the [0001] direction only. Analyses of the high-angle annular dark-field (HAADF) STEM showed that the channels of that sample were partially occupied. It was suggested that the channel species which showed in the images were Fe ions and it was argued on the basis of accompanying mass spectroscopy that all the Fe was in the channels and thus that the colour was induced by channel Fe ions (Arivazhagan et al. 2017). This, however, was later questioned in a recent publication by Knez et al. (2024). Here atomic resolution STEM images of a natural aquamarine crystal are presented, also in the [0001] direction, together with a series of image contrast simulations, leading to the conclusion that the channel occupancy imaged by HAADF STEM is Cs ions, both for the aquamarine sample presented in the paper of Knez et al. (2024) as well as the heliodor sample presented in Arivazhagan et al. (2017). This conclusion is in agreement with assumptions of previous studies which assigned Cs to the $2a$ cavity site in the channels of beryl (e.g., Hawthorne and Černý 1977; Artioli et al. 1993; Gatta et al. 2006).

Inter valence charge transfer (IVCT) between Fe^{2+} and Fe^{3+} ions is thought to contribute to the colour seen in aquamarine (Nassau 1978; Mathew et al. 2000). According to earlier works, these Fe ions would be located in the near vicinity of each other, but multiple sites would be possible (Mathew et al. 2000). In addition to the octahedral site, Fe ions were proposed to substitute in the tetrahedral sites. Although some authors consider the substitution of Be or Si by ferrous Fe unlikely (Viana et al. 2002; Fridrichová et al. 2015), others suggest that the tetrahedral Si site could be occupied by ferric Fe (Andersson 2019). Another, larger and

distorted tetrahedral site with its centre at the coordinates 0.432; 0.344; 0.167 (Andersson 2019), situated next to the Be tetrahedron, is also argued to be the site to accommodate Fe ions as a result of non-isomorphic substitutions (Andersson 2019). These Fe ions would then engage in IVCT, whereas the actual Be site adjacent to such an occupied tetrahedron would be vacant (Andersson 2019). As mentioned earlier, the channel sites are regarded to be another site possibly occupied by Fe ions according to some authors (e.g. Wood and Nassau 1968; Goldman et al. 1978; Blak et al. 1982; Příkryl et al. 2014; Arivazhagan et al. 2017; Bačík and Fridrichová 2019; Bunnag et al. 2020; Shang et al. 2022). IVCT was proposed to occur between the octahedral and channels sites or along the channel sites themselves (Parkin et al. 1977; Goldman et al. 1978). Further studies suggest the 6g interstitial site host Fe ions (Goldman et al. 1978; Groat et al. 2010; Lin et al. 2013.). This site is situated adjacent to the Al octahedron and can thus also enable the close proximity needed for IVCT to occur.

In this study we present atomic resolution HAADF STEM images from a natural aquamarine sample. Images were obtained in the three crystallographic directions [0001], [1-210] and [1-100], two of which have never been shown before for beryl. As with the previous HAADF STEM study on a heliodor sample by Arivazhagan et al. (2017) and the

aquamarine study by Knez et al. (2024), partial channel occupancy could be visualised. The aquamarine used in this study was deliberately chosen to have a much higher Fe content than the heliodor used by Arivazhagan et al. in 2017 on the assumption that a higher Fe content should yield a higher channel occupation ratio if Fe ions were present in the channels to engage in IVCT.

Materials and methods

The aquamarine examined in this study (Fig. 2) originated from Oregon, USA. It was prepared as described in Arivazhagan et al. (2017). In order to guarantee sufficient electrical conductivity and prevent charging effects in the Focused Ion Beam (FIB, Helios G4 UX Dual-Beam by Thermo Fisher Scientific), a 40 nm layer of Pt/Pd was sputter-coated onto the sample prior to FIB preparation. The chosen regions for the TEM lamellae were coated by carbon-based protection layers inside the FIB. The first part of the carbon protection layer was made with e-beam assisted deposition, before a thicker layer (ca. 2 µm thick) was deposited by ion-beam assisted deposition. A tungsten “Easylift” system was used to transfer the cross-section lamellae to a Cu lift-out grid. All coarse thinning was done at 30 kV acceleration voltage for the Ga⁺ ions. To minimize surface damage on either side of the lamellae, lower acceleration voltages of 5 kV and 2 kV were used during the final thinning process. No further coatings were applied to the TEM lamellae. The area depicted in the TEM analyses had a thickness of 40–80 nm as determined by electron energy loss spectroscopy (EELS). EELS data were acquired while scanning over the region of interest using 1 kV/channel dispersion and covering a 2048 eV energy range (including the zero loss peak). EELS spectra were acquired during fast scanning over the region of interest. To avoid beam damage a non-static beam was used. The Log-Ratio method was further employed to determine the relative and absolute thickness. This method has inaccuracies, and a thickness of 40–80 nm is therefore stated in the experimental part even if digital micrograph gives exact values for the sample thickness. The device used for the TEM analyses was a double Cs aberration corrected JEOL ARM 200CF, with a cold field emission gun. The operation voltage was 200 kV. Collection angles for HAADF STEM images were 43–170 mrad, whereas 27.4 mrad was the convergence semi-collection angle. The sample was tilted by 30° inside the TEM to change the analysis direction from [1-100] to [1-210]. The beam current was 21 pA. The dose further depended on the pixel size and the dwell time in each pixel. The dwell time in each pixel was kept constant at 19 µs, while the pixel size varied depending on the magnification used for each image. All images were 2048 × 2048

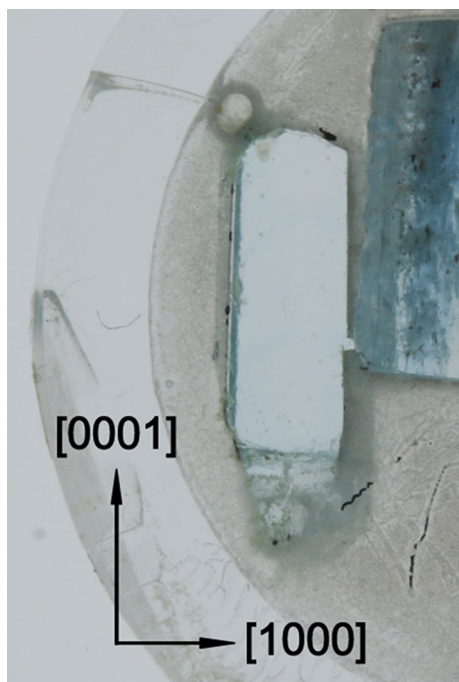


Fig. 2 Sample image of the aquamarine, cast in an acrylic tablet for chemical analyses. A schematic representation of the crystallographic axes is shown in the lower left corner of the image. The aquamarine sample was polished to a plane-parallel slice (with the polished faces parallel to the c-axis of the crystal) and subsequently coated with carbon to ensure electric conductivity for the EPMA analyses. The approximate size of the sample in the photo is 8 × 3 mm

pixels. At very high magnification, these 2048×2048 pixels cover a smaller field of view, whereas at low magnification (i.e. large field of view) the pixel size becomes larger. The beam diameter was typically 0.8 \AA , but the pixel size in high magnification images was much smaller than this. Hence, the smaller the pixel size, the larger the dose per area. In addition, the flyback time was also minimized to avoid a large effective dwell time in the first pixel of every scanned line. The flyback time was reduced from the 500 \mu s default time down to 50 \mu s to avoid amorphization of the sample at the beginning of each scanned line.

Chemical analyses were performed with electron probe microanalysis (EPMA) and laser ablation inductively coupled mass spectrometry (LA-ICP-MS) at the Johannes Gutenberg-University of Mainz, Germany. For both analyses, 10 randomly distributed spots were analysed. In order to avoid analysing inclusions, the spots were placed in areas which seemed homogenous during inspection within the analysis devices. Prior to analyses, the sample was mounted in ClaroCit acrylic. The resulting round acrylic tablet was subsequently coated with carbon to ensure electric conductivity for EPMA (see Fig. 2) before being mounted in a sample holder. The device used for EPMA was a JEOL JXA-8200 SuperProbe (in WDS mode) with lithium fluoride H-type (LIFH) crystal for Fe, Mn and V, thallium acid phthalate (TAP) crystals for Na, Mg, Al, Si, and Rb and pentaerythritol (PET) crystals for K, Ca, Cs, Cr and Ti. The acceleration voltage was 15 kV, the beam current equalled 12 nA and the beam diameter was 10 \mu m . Calibration for EPMA was performed on standards of albite (for Na), diopside (for Mg and Ca) sillimanite (for Al and Si), orthoclase (for K), pyrophanite (for Ti and Mn) eskolaite (for Cr), hematite (for Fe), artificial glass (for Rb) and pollucite (for Cs). LA-ICP-MS analyses were performed with an Agilent 7500ce quadrupole ICP-MS equipped with an ESI New Wave Research ArF laser. The laser wavelength was 193 nm with an energy of 5.56 mJoule/cm^2 . The resulting ablation craters were approximately 75 \mu m in diameter. Calibration and quality control for LA-ICP-MS were carried out on

external reference standard glasses of NIST SRM 610 and NIST SRM 612, as well as BCR. The SiO_2 value determined with EMPA was used as an internal standard. The SiO_2 content is high and comparably stable in silicate minerals such as beryl and therefore even slight variations in SiO_2 content of the respective crystal only have insignificant effects on the final LA-ICP-MS results.

Results

To verify the correct orientation of the sample, electron diffraction images were acquired. Figure 3a-c shows the electron diffraction images in the three directions for which HAADF STEM images were later obtained on the aquamarine. The zone axes for these images are $[0001]$, $[1-210]$ and $[1-100]$. Please note that $[1-210]$ is symmetrically equivalent to $[2-1-10]$ and $[11-20]$. Similarly, $[1-100]$ is symmetrically equivalent to $[10-10]$ and $[01-10]$. The orientations of these directions within the crystal structure of beryl are illustrated in Fig. 1a.

The HAADF images of the beryl sample in the $[0001]$ projection are shown in Fig. 4. Roundish, light-coloured spots can be identified in some of the channels, indicating that these channels are occupied. In addition, some of these spots appear brighter than others. These images are very similar in appearance to those obtained on a heliodor published in Arivazhagan et al. (2017) and another aquamarine samples published in Knez et al. (2024). One of the heliodor images is shown in Fig. 5. Differing ratios of occupied channels relative to the total number of channels can be determined in the images. For the channels in Fig. 4 to be counted, more than 50% of the channel must be visible. Following this criterion, Fig. 4a shows 451 channels, of which only 10 channels are occupied, whereas only 3 channels of the 213 channels are occupied in Fig. 4b. This yields ratios of 2.2% and 1.4%, respectively.

For comparison, Fig. 5a-c shows the HAADF images of the heliodor studied by Arivazhagan et al. (2017). The

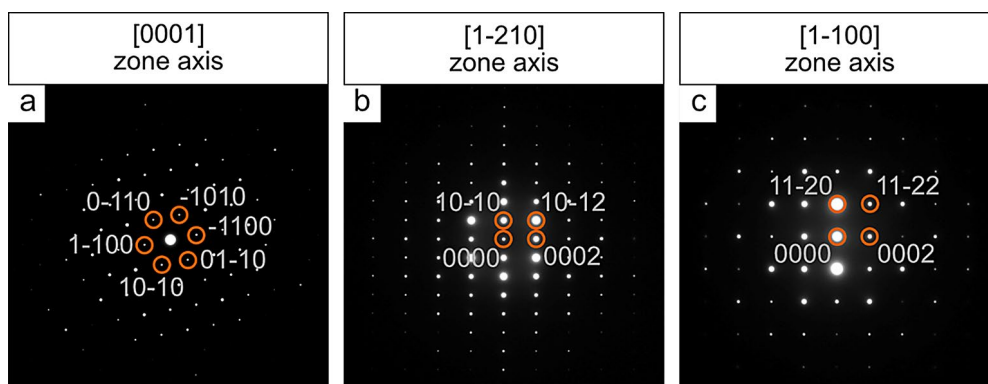


Fig. 3 a-c Electron diffraction images in a the $[0001]$ direction, b the $[1-210]$ direction and c the $[1-100]$ direction

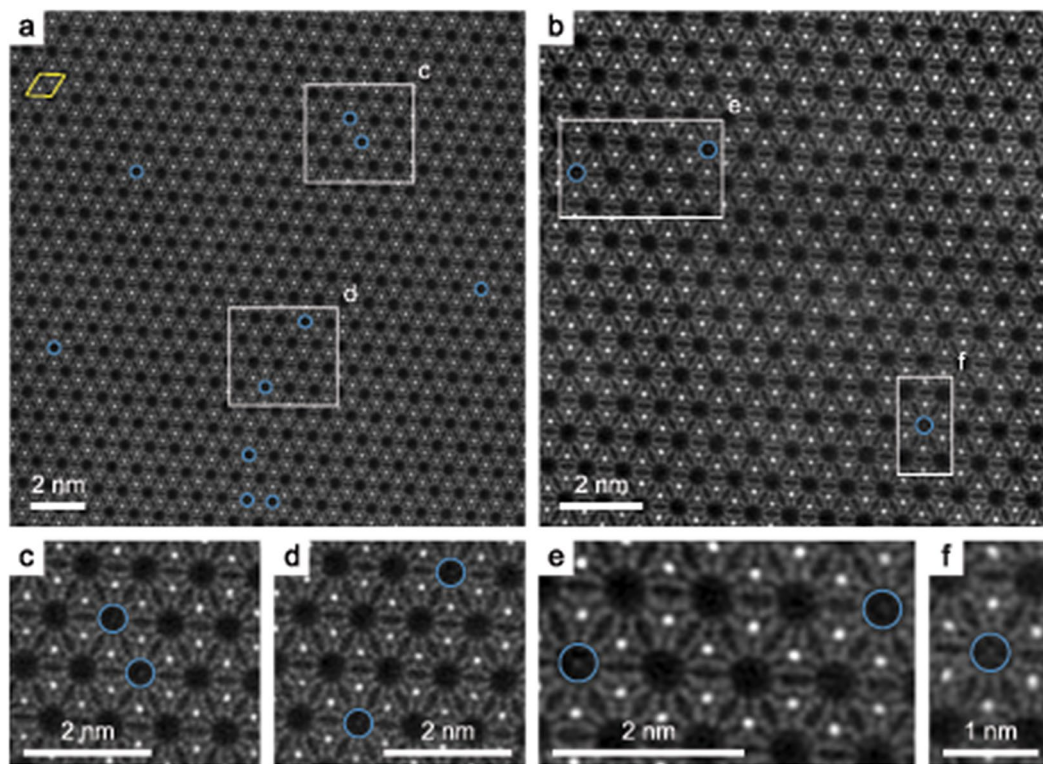


Fig. 4 a-b HAADF images of the aquamarine sample in the [0001] projection. The yellow rhombus shows the unit cell (as indicated in Fig. 1a). The blue circles highlight occupied channels. c-f Enlarged images of a and b

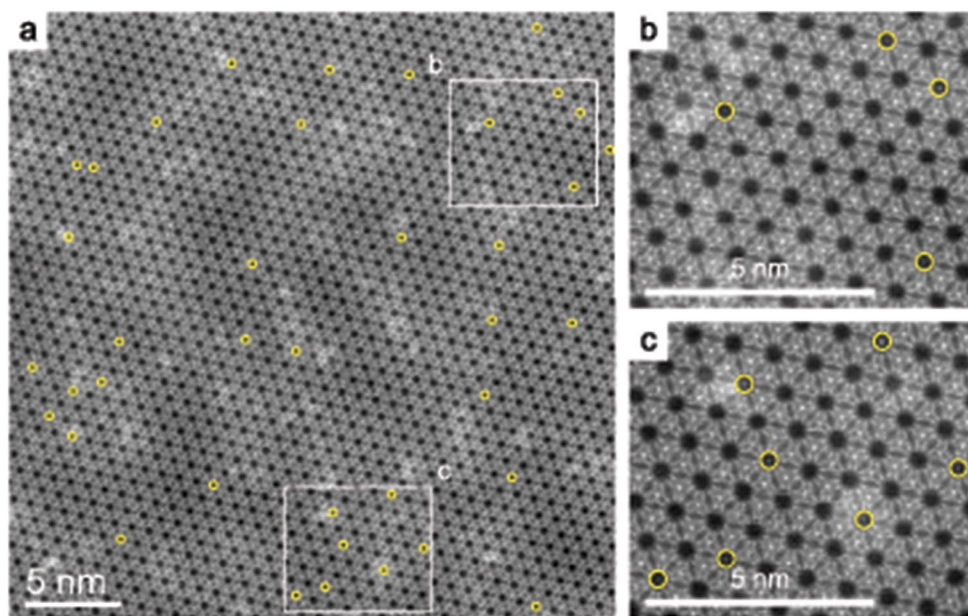


Fig. 5 a HAADF image of the heliodor sample examined in the [0001] projection (modified after Arivazhagan et al. 2017). The yellow circles highlight occupied channels. b-c Enlarged images of a

images resemble those of our aquamarine sample. Figure 5a shows a total of 1399 channels, 39 of which are occupied, yielding a ratio of 2.8%. The uneven contrast of the image (bright, cloudy areas) is likely either caused by redepositions

of the protective sample coating (single atoms or clusters of Pt and C) which had been sputtered off during analyses or by small variations in sample thickness.

In order to determine which positions in the channel are occupied, the aquamarine sample was subsequently analysed in the [1-210] direction. The resulting images are displayed in Fig. 6. This is the first time atomic resolution STEM images have been obtained from a beryl in this orientation. The position of the individual atoms in the channels is revealed as small bright spots which are clearly visible in some of the channels. In the [1-210] direction, the channels are depicted along their length as indicated by the red arrow in Fig. 6a. Thus, they lie flat in the image plane. The channels can be identified as ‘black lines’ running across the images. Figure 6a shows 18 such lines. Since the channels are stacked above each other viewed in this orientation, each channel seen is in fact an accumulation of the signal from several channels. As can be seen, the channel ions reside at the $2a$ channel site. The smaller $2b$ site is covered by the signal of the Si tetrahedra rings (see also Fig. 1b). Thus, occupation of this site is not visible in these images.

Figure 7 shows the HAADF images of the aquamarine in the [1-100] projection. This is the first time images from this projection have been obtained. No bright spots can be seen in the channels since the central area of the channels is covered by the signal of the Al octahedra columns. Hence, in this orientation no channel occupancy could be visualised but these images clearly illustrate the layered structure of beryl perpendicular to the channels.

The results of the chemical analyses using EPMA on the aquamarine of this study and the heliodor of the previous study by Arivazhagan et al. (2017) are displayed in Table 1. The values listed for the heliodor are based on the original analysis files retrieved from the lab where the EPMA analyses were carried out. Comparison diagrams for both samples are shown in Fig. 8. The average and standard deviations

were calculated on the basis of ten spots measured on each sample. The BeO (13 wt%) and H₂O (2 wt%) contents represent fixed values used to improve the PhiRhoZ-correction and were not directly determined with EPMA. The BeO contents were, however, later recalculated from these EPMA and LA-ICP-MS data (Table 2) on the basis of 18 O atoms and 9 tetrahedral cations and using Fe content as FeO and Fe₂O₃, respectively. The EPMA data show that the aquamarine and heliodor have almost identical SiO₂ contents (66.4 wt% as opposed to 66.3 wt% respectively). The amount of Al₂O₃ in our aquamarine is lower (by approximately 0.5 wt%) compared to that in the heliodor, but the Na₂O and FeO contents are higher by about 0.05 wt% and 1 wt%, respectively. All other oxides analysed were close to or below detection limit. Therefore, trace elements were determined with LA-ICP-MS analyses.

Table 2 shows the LA-ICP-MS analyses on our aquamarine and the heliodor sample from Arivazhagan et al. (2017). As with the EPMA analyses, the values listed for the heliodor are based on the original data files provided by the lab at which the LA-ICP-MS analyses were performed. Only the trace elements present at contents greater than 5 ppm in at least one of the two samples are listed. Trace elements below or close to detection limit included Cr and Ni. Be, Mn and Fe were not analysed using LA-ICP-MS, since the error for Be in LA-ICP-MS is high without a calibrated standard, only minor Mn contents were expected and high Fe contents can be determined with EMPA more reliably. Again, the average and standard deviations were calculated on the basis of the ten measurements spots analysed on each sample. The sigma errors (measurement errors) were below 10 ppm for elements at concentrations of 100 ppm or less. For elements present at greater amounts the sigma errors

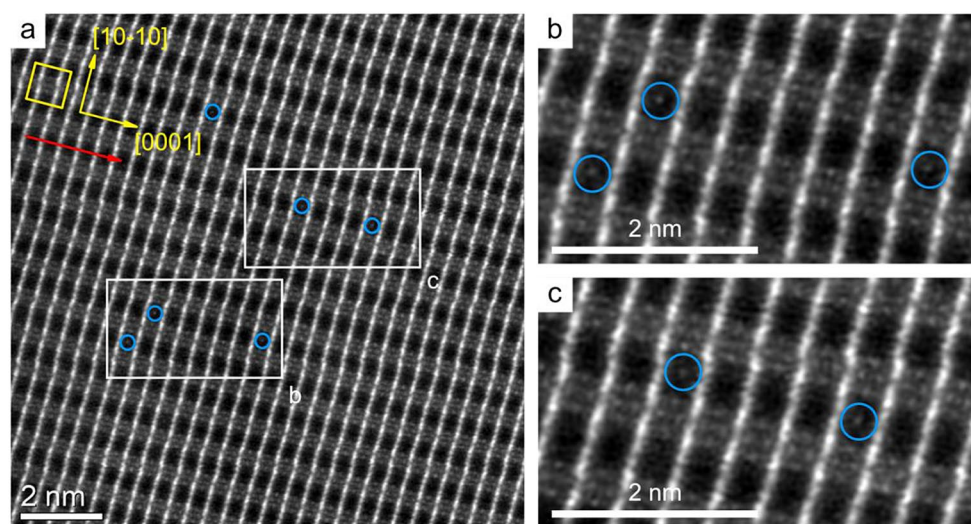


Fig. 6 a HAADF image of the aquamarine sample in the [1-210] projection. The yellow square indicates the unit cell with the corresponding crystallographic directions and indices. The channel direction is

marked with a red arrow. The blue circles highlight channel occupants. **b-c** Enlarged images of **a**

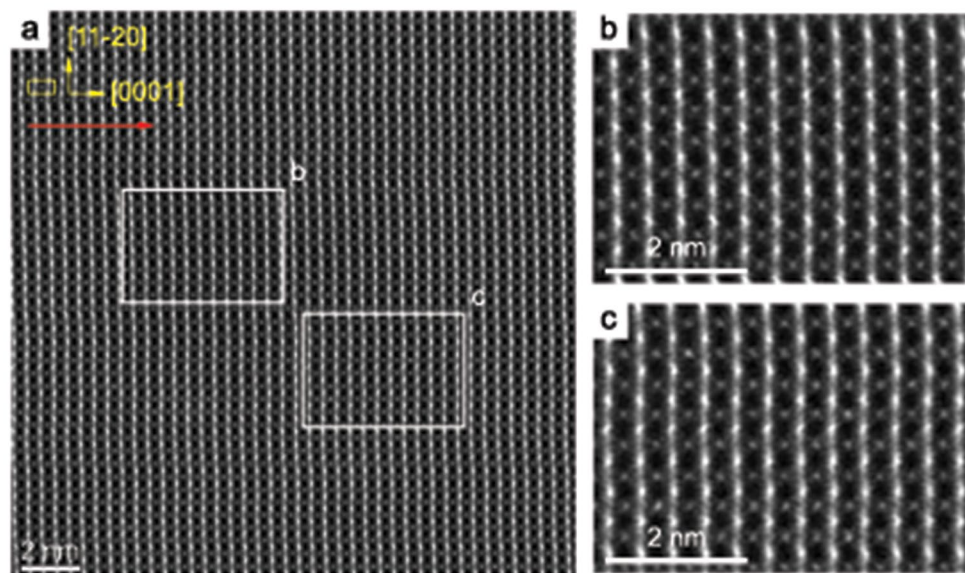


Fig. 7 a HAADF image of the aquamarine sample in the [1-100] projection. The yellow rectangle indicates the unit cell with the corresponding crystallographic directions and indices. The channel direc-

tion is marked with a red arrow. No channel occupancy can be seen in this projection. **b-c** Enlarged images of a

Table 1 Chemical analyses (EPMA) on the aquamarine sample of this study in comparison with those on the heliodor previously investigated by Arivazhagan et al. (2017). The averages and standard deviations were calculated on the basis of 10 measurement spots on each sample

Aquamarine, Oregon, USA			Heliodor, Bin Thuan Province, Vietnam (data from Arivazhagan et al. 2017)		
EPMA			EPMA		
Oxide	Average [wt%]	Standard deviation [wt%]	Oxide	Average [wt%]	Standard deviation [wt%]
SiO ₂	66.4	0.18	SiO ₂	66.3	0.20
Al ₂ O ₃	17.6	0.19	Al ₂ O ₃	18.2	0.12
FeO	1.2	0.15	FeO	0.2	0.03
BeO* (fix)	13	N/A	BeO* (fix)	13	N/A
MnO	0.02	0.01	MnO	0.01	0.01
Na ₂ O	0.14	0.03	Na ₂ O	0.09	0.02
H ₂ O* (fix)	2	N/A	H ₂ O* (fix)	2	N/A

* not determined, N/A = not applicable, recalculated Fe₂O₃ values: 1.4 wt% (aquamarine) and 0.2 wt% (heliodor), recalculated BeO values (based on 18 O atoms, 9 tetrahedral cations and including element contents determined with LA-ICP-MS, see Table 2): 13.5 wt% (aquamarine with Fe content as FeO) and 13.4 wt% (heliodor with Fe content as FeO), 13.7 wt% (aquamarine with Fe content as Fe₂O₃) and 13.5 wt% (heliodor with Fe content as Fe₂O₃)

ranged between a few ppm to about 50 ppm. Bar diagrams comparing the different trace elements are shown in Fig. 9a-l. The average contents of Mg, K and V are higher in the aquamarine. The values for most other elements are similar or overlap within the standard deviation. Li, Zn and Cs are the only elements for which the average amounts are higher in the heliodor from Arivazhagan et al. (2017) than in our sample.

To determine the occupation of the octahedral Al position in this aquamarine and the heliodor from Arivazhagan et al. (2017), the atoms per formula unit (apfu) values (Table 3) were calculated using the chemical data given in Tables 1 and 2 (with the exception of the H₂O content). For Be the recalculated BeO values were used. The calculations are

based on 18 oxygens per formula unit. Since the precise ratio of ferrous (Fe²⁺) to ferric (Fe³⁺) Fe is unknown, two separate apfu calculations were performed for each sample using FeO and Fe₂O₃, respectively. Thus, the calculations represent extreme cases since the Fe content was treated as either being all ferrous or all ferric, respectively. Because of the high Na content, the apfu for Na are based on the values determined via EPMA. In case of the aquamarine, the calculations show that Mn, Li, K, Ca, Sc, Ti, V, Zn, Ga, Rb and Cs are low compared with the other non-formula elements Fe, Mg and Na. In addition, there is slightly more Si than the six apfu needed for the beryl formula. However, the apfu values are lower than the ideal number in case of Al and Be. Apfu were also calculated for the heliodor investigated

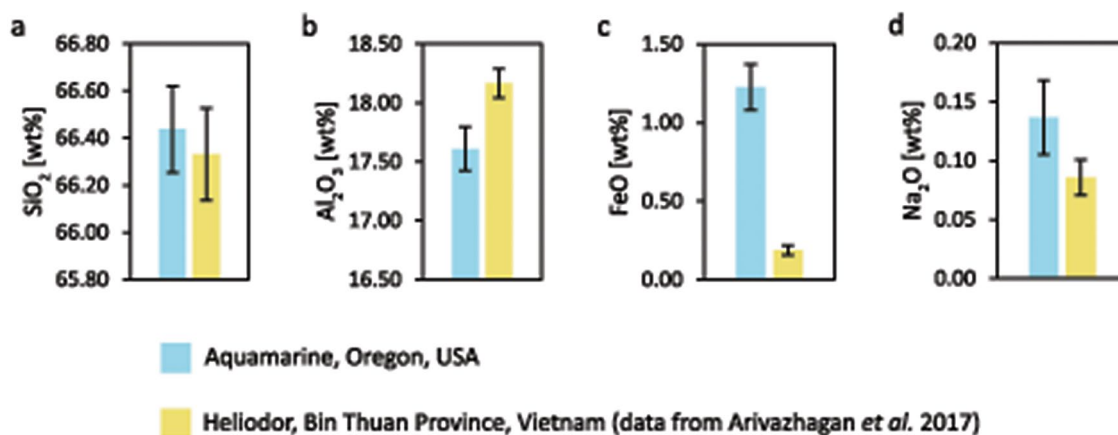


Fig. 8 a–d Average chemical composition (determined by EPMA) of the aquamarine of this study in comparison to the data on a heliodor studied previously (data from Arivazhagan et al. 2017). The error bars show the standard deviation

Table 2 Chemical analyses (LA-ICP-MS) on the aquamarine sample of this study in comparison with those on the heliodor previously investigated by Arivazhagan et al. (2017). The averages and standard deviations were calculated on the basis of 10 measurement spots on each sample

Aquamarine, Oregon, USA			Heliodor, Bin Thuan Province, Vietnam (data from Arivazhagan et al. 2017)		
LA-ICP-MS			LA-ICP-MS		
Element	Average [ppm]	Standard deviation [ppm]	Element	Average [ppm]	Standard deviation [ppm]
Li	65	10	Li	149	66
Na	1061	229	Na	600	205
Mg	562	140	Mg	29	8
K	124	41	K	22	8
Ca	284	34	Ca	227	37
Sc	166	57	Sc	74	36
Ti	49	40	Ti	25	9
V	57	8	V	3	1
Zn	57	9	Zn	83	31
Ga	28	2	Ga	27	7
Rb	38	22	Rb	12	3
Cs	379	138	Cs	458	99

in Arivazhagan et al. (2017). Again most non-formula elements (Mn, K, Ca, Sc, Ti, V, Ga, Rb) are low, but the apfu for Li, Zn and Cs are higher compared to the values determined for the aquamarine. The heliodor sample also shows excess Si and a lack of Be and Al atoms per formula unit.

The ratios of the apfu of elements which can occupy the octahedral position in beryl (transition metals and Mg) are shown in Fig. 10. For these diagrams only those elements with a sufficient apfu value (equal to or higher than 0.001 apfu) are shown as individual sections in the bar diagrams, whereas the apfu of the remaining elements are summed up. In the aquamarine the octahedral position can mainly be filled with Al, Fe, Mg, Mn and Sc. When all Fe is treated as ferrous, there is a slight deficiency of 0.002 apfu at the octahedral position. If all Fe is treated as being ferric, the deficiency is greater (0.012 apfu). In contrast to this, the octahedral site in the heliodor can mainly be filled by Al and Fe only. The contribution of the remaining elements to

the occupation of the octahedral site in the heliodor is small. Hence, the Al site remains under-occupied to a greater extent in the heliodor than the aquamarine.

Discussion

From the [0001] and [1-210] projections in this new specimen it is clear that only a small fraction of channels is occupied, similar to what has been observed before (Arivazhagan et al. 2017; Knez et al. 2024). The varying degrees of brightness of the spots seen in the channel along the [0001] projection may be due to several reasons. It could be the result of different scattering potentials between different channel species. Another reason could be the depth of the channel itself (see Knez et al. 2024). The images shown represent projections of a thin slab of beryl of about 40–80 nm thickness. Less bright spots may be caused by ions situated

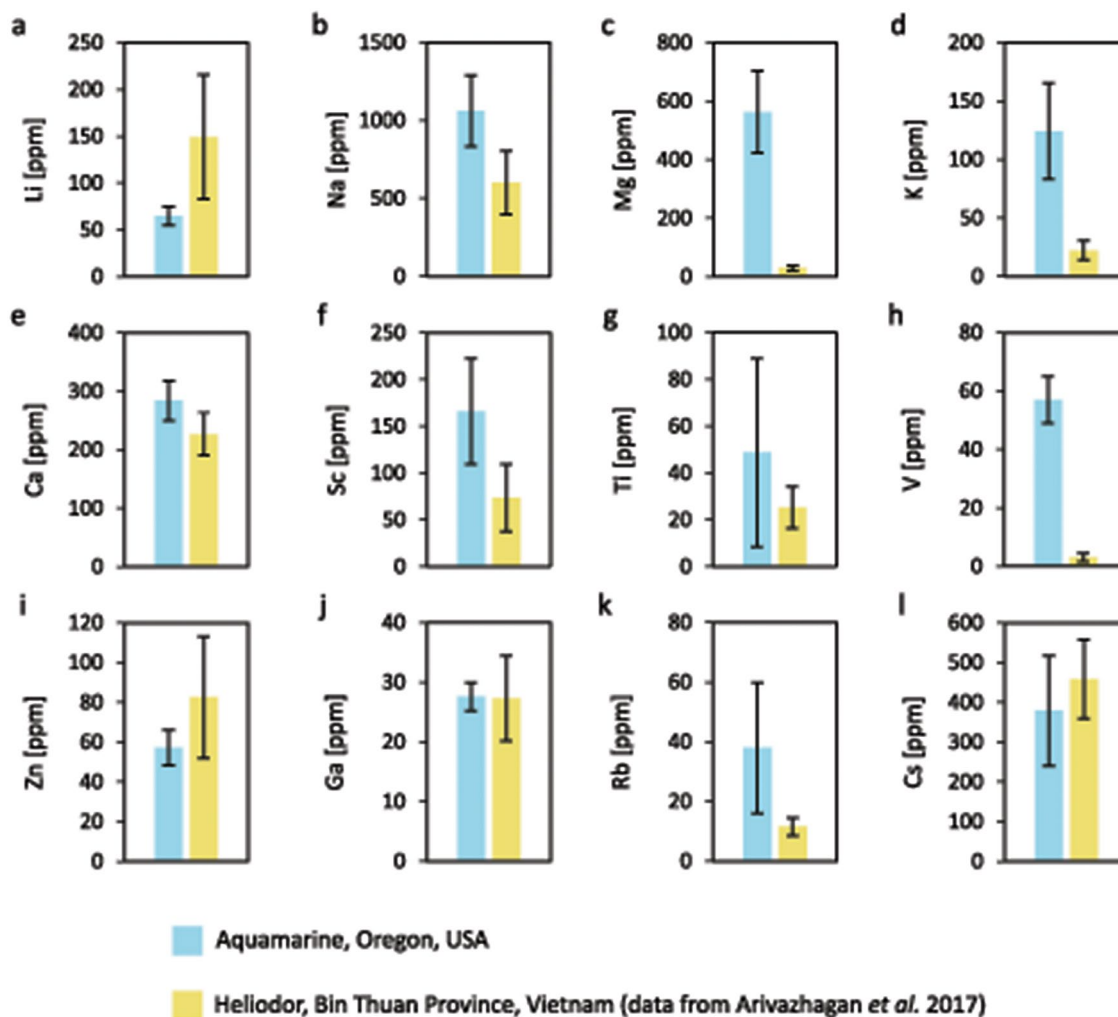


Fig. 9 a–i Average chemical composition (determined by LA-ICP-MS) of the aquamarine of this study in comparison to a heliodor studied previously (data from Arivazhagan et al. 2017). The error bars show the standard deviation

deeper within the channel, yielding an apparently weaker signal. Alternatively, brighter spots could be caused by ions stacked above each other along the length of the same channel, causing their scattering signals to accumulate. Although the same channels appear to be occupied multiple times in the $[1-210]$ images, it has to be taken into account that this projection represents the accumulated signal of several channels stacked above each other. Therefore, channel species in the same channel orientation may occupy different channels. Since the structure is seen along the a - or b -axes (see Fig. 1) in case of the $[1-210]$ projection, the signal of the Si tetrahedra rings masks the signals of any particles possibly present at the $2b$ site within these rings. Therefore, only the occupation of the $2a$ site can be seen. Large molecules like H_2O and CO_2 , but also larger alkalis, such as Cs, Rb or K, occupy the larger $2a$ site (Hawthorne and Černý 1977; Charoy et al. 1996; Gatta et al. 2006; McMillan et al. 2006). Smaller ions like Na can be present at the $2b$ ring site

(Hawthorne and Černý 1977; Gatta et al. 2006; McMillan et al. 2006). Yet, Na may occupy the $2a$ site in some beryls as well, depending on the general alkali content and the presence of H_2O within beryl (Mashkovtsev and Solntsev 2002; Gatta et al. 2006). Taking the various degrees of spot brightness in the images of the $[0001]$ direction into account and under the assumption that both channel sites are partially occupied in this aquamarine, it is possible that more than one channel species is seen in the $[0001]$ projection. However, a smaller amount of channels is depicted within the same field of view in the $[1-210]$ compared to the $[0001]$ orientation. In the $[1-210]$ plane, the channels are seen along their length, creating a set of ‘lines’ in these images. This set only consists of 18 lines in Fig. 6a. Although the channels are stacked above each other in this direction, primarily the signal of the upper channel layers is seen in HAADF STEM. Even when taking the signal depth into account, it is likely that the signal in the $[1-210]$ projections in Fig. 6a results

Table 3 Calculated atoms per formula unit (apfu) on the basis of the EPMA and LA-ICP-MS analyses shown in Tables 1 and 2. The calculations were performed with the total Fe content being Fe³⁺ or Fe²⁺, respectively, and are based on 18 oxygens per formula unit. All values are rounded to four decimal places

Aquamarine, Oregon, USA				Heliodor, Bin Thuan Province, Vietnam			
Atom	Apfu	Atom	Apfu	Atom	Apfu	Atom	Apfu
Al	1.8871	Al	1.8774	Al	1.9519	Al	1.9504
Si	6.0412	Si	6.0102	Si	6.0476	Si	6.0428
Na	0.0241	Na	0.0240	Na	0.0151	Na	0.0151
Be	2.9537	Be	2.9848	Be	2.9406	Be	2.9454
Fe ²⁺	0.0931	Fe ³⁺	0.0926	Fe ²⁺	0.0142	Fe ³⁺	0.0142
Mn	0.0014	Mn	0.0014	Mn	0.0007	Mn	0.0007
Li	0.0051	Li	0.0051	Li	0.0118	Li	0.0118
Mg	0.0126	Mg	0.0126	Mg	0.0007	Mg	0.0007
K	0.0017	K	0.0017	K	0.0003	K	0.0003
Ca	0.0039	Ca	0.0039	Ca	0.0031	Ca	0.0031
Sc	0.0020	Sc	0.0020	Sc	0.0009	Sc	0.0009
Ti	0.0006	Ti	0.0006	Ti	0.0003	Ti	0.0003
V	0.0006	V	0.0006	V	0.0000	V	0.0000
Zn	0.0005	Zn	0.0005	Zn	0.0007	Zn	0.0007
Ga	0.0002	Ga	0.0002	Ga	0.0002	Ga	0.0002
Rb	0.0002	Rb	0.0002	Rb	0.0001	Rb	0.0001
Cs	0.0016	Cs	0.0016	Cs	0.0019	Cs	0.0019

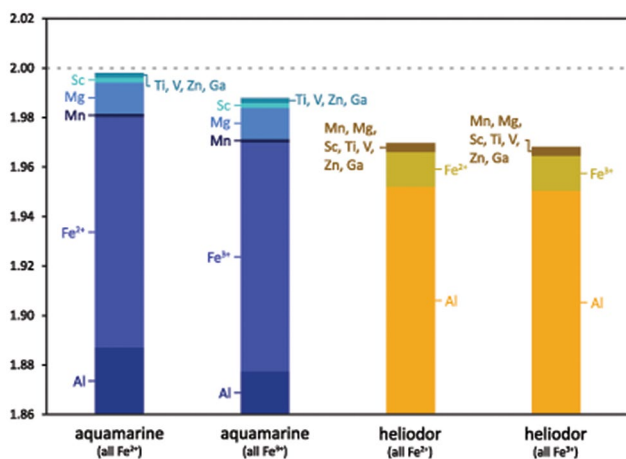


Fig. 10 Comparison of the apfu calculations for elements which would be able to occupy the octahedral position in the aquamarine and heliodor. The left column for each sample shows the apfu ratios with Fe being all ferrous, whereas the right column for each sample depicts the apfu ratios for Fe being all ferric. The dashed, grey line highlights where the ideal value of 2 for the octahedral position is reached in accordance with the chemical formula of beryl ($\text{Be}_3\text{Al}_2[\text{Si}_6\text{O}_{18}]$). The data for the calculations of the apfu for heliodor were taken from Arivazhagan et al. (2017)

from fewer channels stacked above each other than the total number of channel ‘openings’ visible in the [0001] projections in Fig. 4a–b within the same field of view. Thus, the number of channel ions seen in both projections could be similar. Therefore, it is also possible that only one channel species is seen in both projections.

Na^+ is a larger ion than Fe^{2+} or Fe^{3+} (Shannon 1976). The 2a and 2b channel sites would both be large enough for

either ion to reside at. However, the amount of FeO in the aquamarine of this study is about 6 times higher than that of the previous heliodor. Yet, the ratio of occupied channels to total amount of channels in the [0001] projections ranged between 1.4% and 2.2% in the aquamarine. This is lower than the approximately 2.8% of occupied channels seen in the heliodor studied previously by Arivazhagan et al. (2017). However, it has to be noted that these statistics are based on only a couple of images for each sample and small occupancy numbers. Furthermore, a couple of additional factors have to be considered as well. The aquamarine sample was thicker (40–80 nm as opposed to the 40±20 nm for the heliodor in Arivazhagan et al. (2017). Channel species deeper within the channel may not yield a sufficiently high enough signal to be clearly identified as the signal seen in HAADF STEM results from the upper layers only. The bright areas in the heliodor image indicate redeposition of the protective coating during analyses or a variation in sample thickness. In addition, the images on the heliodor of the previous study were noisier, making the distinction between occupied channels and background noise more difficult. Although the images taken on the aquamarine were less noisy than those taken on the heliodor, they depicted a smaller field of view, making the statistical error larger. Moreover, multiple occupations of the same channel can occur. Both ratios of occupation may therefore be more similar or even overlap.

The apfu calculations show that the Fe content correlates with the lack of Al at the octahedral site. In the extreme case calculation of all Fe being ferrous, the entire amount of Mg and Fe would be needed to counteract the lack of

Al in the aquamarine. Sc and Mn do not contribute much to the substitution. Hence, the octahedral site is very close to the ideal apfu value (1.998 apfu as opposed to the ideal 2.000 apfu). Treating the entire Fe content as ferric in this aquamarine would also yield a slight deficiency of apfu for the octahedral site (deficiency of 0.012 apfu). In reality, this deficiency would be lower since the colour-causing process in aquamarine is thought to be rooted in IVCT between Fe^{2+} and Fe^{3+} and both Fe ions should therefore be present in the sample. Thus, the actual scenario should lie between these two extreme cases of all Fe being ferrous and all Fe being ferric. According to some studies, Fe ions might enter the channel and IVCT could then take place between octahedral Fe and channel Fe ions (Parkin et al. 1977; Goldman et al. 1978). In addition, Fe ions may also be found at the 6g interstitial site (Goldman et al. 1978; Groat et al. 2010; Lin et al. 2013) and may simultaneously occupy this site and the octahedral site within beryl (Goldman et al. 1978; Lin et al. 2013), enabling IVCT between them. Since there is a lack of Al and a slight deficiency of atoms to substitute for it based on the apfu calculations, it seems more likely for Fe to fill the lattice positions than to leave them vacant to enter the channels. Substitution of lattice components (Be^{2+} , Si^{4+} and Al^{3+}) by lower-valent ions causes charge deficiencies, which are balanced by alkalis in the channels. The heliodor previously studied by Arivazhagan et al. (2017) shows a stronger under-occupation for both extreme scenarios of all Fe being ferrous and all Fe being ferric, respectively. In this case, it also seems more likely for Fe to be incorporated in the lattice to build the framework. The remaining deficiency of charges at the octahedral site would need to be balanced by alkalis. Therefore, the signal from channel species in the HAADF images of the heliodor and our aquamarine is likely caused by alkalis. The average Na, K and Rb contents are lower in the heliodor than in the aquamarine. However, the average amounts of Li and Cs are higher. Li and Na are too light to produce a signal in the HAADF images. K and Rb are not abundant enough in the two beryl samples to explain the amount of occupied channels. In addition, the concentrations of both alkalis are higher in the aquamarine than in the heliodor and therefore cannot explain the higher amount of occupied channels in the heliodor compared to that in the aquamarine. The average content of Cs in the aquamarine, however, is smaller than that in the heliodor. The average Cs content in the aquamarine (379 ppm) is only 79% of the Cs content of the heliodor (458 ppm). Similarly, the maximum ratio of occupied to total channels in the aquamarine (2.2%) is only 82% of the ratio seen in the heliodor (2.8%). In combination with the possibility of only one channel species observed (as discussed earlier) and the apfu calculations and correlations, it is highly plausible that the signal from channel species in the HAADF images arises from Cs ions.

This is in contrast to previous conclusions by Arivazhagan et al. (2017), but it is consistent with the deductions made by Knez et al. (2024) who also attributed the signal observed by Arivazhagan et al. (2017) to Cs ions in the channels based on relative HAADF intensity calculations.

It should be noted that although the chemical analyses and the HAADF STEM images were performed on the same beryl, it is impossible to analyse identical areas of the sample in all these measurements. Channel species may be unevenly distributed across the sample causing discrepancies between the chemical analyses and the observations in HAADF STEM. The area observed with HAADF STEM may thus not be representative of the entire crystal, especially because of the small size of the field of view. This uneven distribution of chemical components, called zoning, is a phenomenon commonly observed in natural minerals, including beryl (Scandale and Lucchesi 2000; Hill and Sirbescu 2022).

Conclusion and outlook

In this paper, we present the first atomic resolution images (HAADF STEM) of a beryl crystal for all the fundamental crystal orientations. The images in the [1000] and [1-210] directions reveal channel occupying atoms visible as bright spots. The images in the [1-210] direction directly show that ions reside at the $2a$ cavity site (the $2b$ site is covered by the signal of the Si tetrahedra rings). By combining the occupancy ratios from the images with the apfu analyses we are able to show that the imaged atoms are most likely Cs, in agreement with the results from Knez et al. (2024). Our paper demonstrates the power of the STEM technique as a novel tool for mineralogy. Natural materials offer a particular challenge to microscopical investigation, because only a very small area can be investigated in microscopy. The expense, time and high spatial resolution required for atomic resolution transmission electron microscopy make it at present practically impossible to investigate a large number of samples collected in different areas to ensure statistics. Therefore, future work should include a systematic investigation of synthetically grown beryls. For these, the growth conditions can be controlled, including the availability of elements, such as Fe and Na. To fully clarify the nature of the channel species, elemental analyses on the individual spots in the channels should also be applied once the STEM technique is evolved enough.

Acknowledgements The authors would like to thank Nora Groschopf and Stephan Buhre for the EPMA and Regina Mertz for the LA-ICP-MS analyses. Thank you also to Regina Mertz, Jana David, Mareike Leiter and Pascal Hamsch for their invaluable support in obtaining the original data sets. The authors would also like to thank the three anonymous reviewers for their helpful comments.

Author contributions F.S., B.H. and R.B. designed the experiments. The samples were prepared by P.E.V. and subsequently analysed by F.S., A.T.J.v.H. and P.E.V. in STEM. All authors contributed to the data interpretation. C.H. wrote the first manuscript draft and performed all data evaluations. Comments and changes to the manuscript were made by all authors.

Funding This project has received funding from the European Union's Horizon 2020 research and innovation programme under grant agreement No 823717 – ESTEEM3. Support by the Research Council of Norway to NORTEM (197405) and NorFab (295864) is acknowledged. This project was also partly funded by a collaboration between Johannes Gutenberg-University Mainz, Germany and Idar-Oberstein, Germany. Open Access funding enabled and organized by Projekt DEAL.

Data availability No datasets were generated or analysed during the current study.

Declarations

Competing interests The authors declare no competing interests.

Open Access This article is licensed under a Creative Commons Attribution 4.0 International License, which permits use, sharing, adaptation, distribution and reproduction in any medium or format, as long as you give appropriate credit to the original author(s) and the source, provide a link to the Creative Commons licence, and indicate if changes were made. The images or other third party material in this article are included in the article's Creative Commons licence, unless indicated otherwise in a credit line to the material. If material is not included in the article's Creative Commons licence and your intended use is not permitted by statutory regulation or exceeds the permitted use, you will need to obtain permission directly from the copyright holder. To view a copy of this licence, visit <http://creativecommons.org/licenses/by/4.0/>.

References

- Andersson LO (2013) The yellow color center and trapped electrons in beryl. *Can Mineral* 51:15–25. <https://doi.org/10.3749/canmin.51.1.15>
- Andersson LO (2019) Comments on Beryl Colors and on other observations regarding Iron-containing beryls. *Can Mineral* 57:551–566. <https://doi.org/10.3749/canmin.1900021>
- Arivazhagan V, Schmitz FD, Vullum PE, Van Helvoort ATJ, Holst B (2017) Atomic resolution imaging of beryl: an investigation of the nano-channel occupation. *J Microsc* 265:245–250. <https://doi.org/10.1111/jmi.12493>
- Artioli G, Rinaldi R, Stahl K, Zanazzi PF (1993) Structure refinements of beryl by single-crystal neutron and X-ray diffraction. *Am Mineral* 78:762–768
- Bačík P, Fridrichová J (2019) The site occupancy Assessment in Beryl based on bond-length constraints. *Minerals* 9:641. <https://doi.org/10.3390/min9100641>
- Blak AR, Isotani S, Watanabe S (1982) Optical absorption and electron spin resonance in blue and green natural beryl. *Phys Chem Miner* 8:161–166. <https://doi.org/10.1007/BF00308238>
- Bragg W.L., West J (1926) The structure of beryl, $3\text{Al}_2\text{Si}_6\text{O}_{18}$. *Proc Royal Soc Lond Ser Containing Papers Math Phys Character* 111:691–714. <https://doi.org/10.1098/rspa.1926.0088>
- Bunnag N, Kasri B, Setwong W, Sirisurawong E, Chotsawat M, Chirawatkul P, Saiyasombat C (2020) Study of Fe ions in aquamarine and the effect of dichroism as seen using UV–Vis, NIR and x-ray. *Radiat Phys Chem* 177:109107. <https://doi.org/10.1016/j.radphyschem.2020.109107>
- Burns RG (1993) Mineralogical application of crystal theory. Cambridge University Press, p 551
- Buseck PR, Sumio I (1974) High resolution electron microscopy of silicates. *Am Mineralogist: J Earth Planet Mater* 59:1–21
- Charoy B, de Donato P, Barres O, Pinto-Coelho C (1996) Channel occupancy in an alkali-poor beryl from Serra Branca (Goias, Brazil); spectroscopic characterization. *Am Mineral* 81:395–403. <https://doi.org/10.2138/am-1996-3-414>
- Fridrichová J, Bačík P, Rusinová P, Antal P, Škoda R, Bizovská V, Miglierini M (2015) Optical and crystal-chemical changes in aquamarines and yellow beryls from Thanh Hoa Province, Vietnam induced by heat treatment. *Phys Chem Miner* 42:287–302. <https://doi.org/10.1007/s00269-014-0719-4>
- Fridrichová J, Bačík P, Ertl A, Wildner M, Dekan J, Miglierini M (2018) Jahn-Teller distortion of Mn^{3+} -occupied octahedra in red beryl from Utah indicated by optical spectroscopy. *J Mol Struct* 1152:79–86. <https://doi.org/10.1016/j.molstruc.2017.09.081>
- Fritsch E, Rossman GR, and others (1988) An update on color in gems. Part 2: colors involving multiple atoms and color centers. *Gems Gemology* 24:3–15
- Gatta GD, Nestola F, Bromiley GD, Mattauch S (2006) The real topological configuration of the extra-framework content in alkali-poor beryl: a multi-methodological study. *Am Mineral* 91:29–34. <https://doi.org/10.2138/am.2006.1896>
- Gaudry E, Cabaret D et al (2007) Relaxations around the substitutional chromium site in emerald: X-ray absorption experiments and density functional calculations. *Phys Rev B* 76:094110. <https://doi.org/10.1103/PhysRevB.76.094110>
- Gibbs GV, Breck DW, Meagher EP (1968) Structural refinement of hydrous and anhydrous synthetic beryl, $\text{Al}_2(\text{Be}_3\text{Si}_6)\text{O}_{18}$ and emerald, $\text{Al}_1.9\text{Cr}_{0.1}(\text{Be}_3\text{Si}_6)\text{O}_{18}$. *Lithos* 1:275–285. [https://doi.org/10.1016/S0024-4937\(68\)80044-1](https://doi.org/10.1016/S0024-4937(68)80044-1)
- Goldman DS, Rossman GR, Parkin KM (1978) Channel constituents in beryl. *Phys Chem Miner* 3:225–235. <https://doi.org/10.1007/BF00633572>
- Groat LA, Rossman GR, Dyar MD, Turner D, Piccoli PMB, Schultz AJ, Ottolini L (2010) Crystal chemistry of dark blue aquamarine from the True Blue Showing, Yukon Territory, Canada. *Can Mineral* 48:597–613. <https://doi.org/10.3749/canmin.48.3.597>
- Hawthorne F, Černý P (1977) The alkali-metal positions in Cs-Li beryl. *Can Mineral* 15:414–421
- Hill T, Sirbescu M (2022) Micro-XRF mapping of chemically zoned Beryl: Fast, non-destructive, and Precise. *Microsc Microanal* 28:624–628. <https://doi.org/10.1017/S1431927622003038>
- Knez D, Gspan C et al (2024) Three-dimensional distribution of individual atoms in the channels of beryl. *Commun Mater* 5:19
- Lin J, Chen N, Huang D, Pan Y (2013) Iron pairs in beryl: new insights from electron paramagnetic resonance, synchrotron X-ray absorption spectroscopy, and ab initio calculations. *Am Mineral* 98:1745–1753. <https://doi.org/10.2138/am.2013.4472>
- Łodziński M, Sitarz M, Stec K, Kozanecki M, Fojud Z, Jurga S (2005) ICP, IR, Raman, NMR investigations of beryls from pegmatites of the Sudety Mts. *J Mol Struct* 744–747(1005–1015). <https://doi.org/10.1016/j.molstruc.2004.12.042>
- Mashkovtsev RI, Solntsev VP (2002) Channel constituents in synthetic beryl: ammonium. *Phys Chem Miner* 29:65–71. <https://doi.org/10.1007/s002690100206>
- Mathew G, Karanth RV, Rao TKG, Deshpande RS (2000) Colouration in Natural beryls: a Spectroscopic Investigation. *J Geol Soc India* 56:285–303

- McMillan NJ, McManus CE, Harmon RS, De Lucia FC, Miziolek AW (2006) Laser-induced breakdown spectroscopy analysis of complex silicate minerals—beryl. *Anal Bioanal Chem* 385:263–271. <https://doi.org/10.1007/s00216-006-0374-9>
- Morosin B (1972) Structure and thermal expansion of beryl. *Acta Crystallogr Sect B Struct Crystallogr Cryst Chem* 28:1899–1903. <https://doi.org/10.1107/S0567740872005199>
- Nassau K (1978) The origins of color in minerals. *Am Mineral* 63:219–229
- Nassau K, Wood DL (1968) An examination of red beryl from Utah. *Am Mineral* 53:801–806
- Parkin KM, Loeffler BM, Burns RG (1977) Mössbauer spectra of kyanite, aquamarine, and cordierite showing intervalence charge transfer. *Phys Chem Miner* 1:301–311. <https://doi.org/10.1007/BF00307569>
- Přikryl J, Novák M, Filip J, Gadas P, Galiová MV (2014) Iron+magnesium-bearing beryl from granitic pegmatites: an EMPA, LA-ICP-MS, Mössbauer spectroscopy and powder XRD study. *Can Mineral* 52:271–284. <https://doi.org/10.3749/canmin.52.2.271>
- Scandale E, Lucchesi S (2000) Growth and sector zoning in a beryl crystal. *Eur J Mineral* 12:357–366. <https://doi.org/10.1127/ejm/12/2/0357>
- Shang Y, Guo Y, Tang J (2022) Spectroscopy and chromaticity characterization of yellow to light-blue iron-containing beryl. *Sci Rep* 12:10765. <https://doi.org/10.1038/s41598-022-11916-z>
- Shannon RD (1976) Revised effective ionic radii and systematic studies of interatomic distances in halides and chalcogenides. *Acta Crystallogr Sect A* 32:751–767. <https://doi.org/10.1107/S0567739476001551>
- Spinolo G, Fontana I, Galli A (2007) Optical absorption spectra of Fe²⁺ and Fe³⁺ in beryl crystals. *Phys Status Solidi (b)* 244:4660–4668. <https://doi.org/10.1002/pssb.200743102>
- Taran MN, Vyshnevskiy OA (2019) Be, Fe²⁺-substitution in natural beryl: an optical absorption spectroscopy study. *Phys Chem Miner* 46:795–806. <https://doi.org/10.1007/s00269-019-01040-2>
- Viana RR, da Costa GM, De Grave E, Stern WB, Jordt-Evangelista H (2002) Characterization of beryl (aquamarine variety) by Mössbauer spectroscopy. *Phys Chem Miner* 29:78–86. <https://doi.org/10.1007/s002690100210>
- Wang P, Gray TP et al (2021) Mineralogical classification and crystal water characterisation of beryl from the W–Sn–Be occurrence of Xuebaoding, Sichuan province, western China. *Mineral Mag* 85:172–188. <https://doi.org/10.1180/mgm.2021.13>
- Wood DL, Nassau K (1968) The characterization of beryl and emerald by visible and infrared absorption spectroscopy. *Am Mineral* 53:777–800

Publisher's Note Springer Nature remains neutral with regard to jurisdictional claims in published maps and institutional affiliations.